Volume 1 | Number 1 | Jan 2013 | Pages 1–100

Dalton Transactions

An international journal of inorganic chemistry
www.rsc.org/dalton

ROYAL SOCIETY OF CHEMISTRY

This is an *Accepted Manuscript*, which has been through the Royal Society of Chemistry peer review process and has been accepted for publication.

Accepted Manuscripts are published online shortly after acceptance, before technical editing, formatting and proof reading. Using this free service, authors can make their results available to the community, in citable form, before we publish the edited article. We will replace this *Accepted Manuscript* with the edited and formatted *Advance Article* as soon as it is available.

You can find more information about *Accepted Manuscripts* in the **Information for Authors**.

Please note that technical editing may introduce minor changes to the text and/or graphics, which may alter content. The journal's standard **Terms & Conditions** and the **Ethical guidelines** still apply. In no event shall the Royal Society of Chemistry be held responsible for any errors or omissions in this *Accepted Manuscript* or any consequences arising from the use of any information it contains.

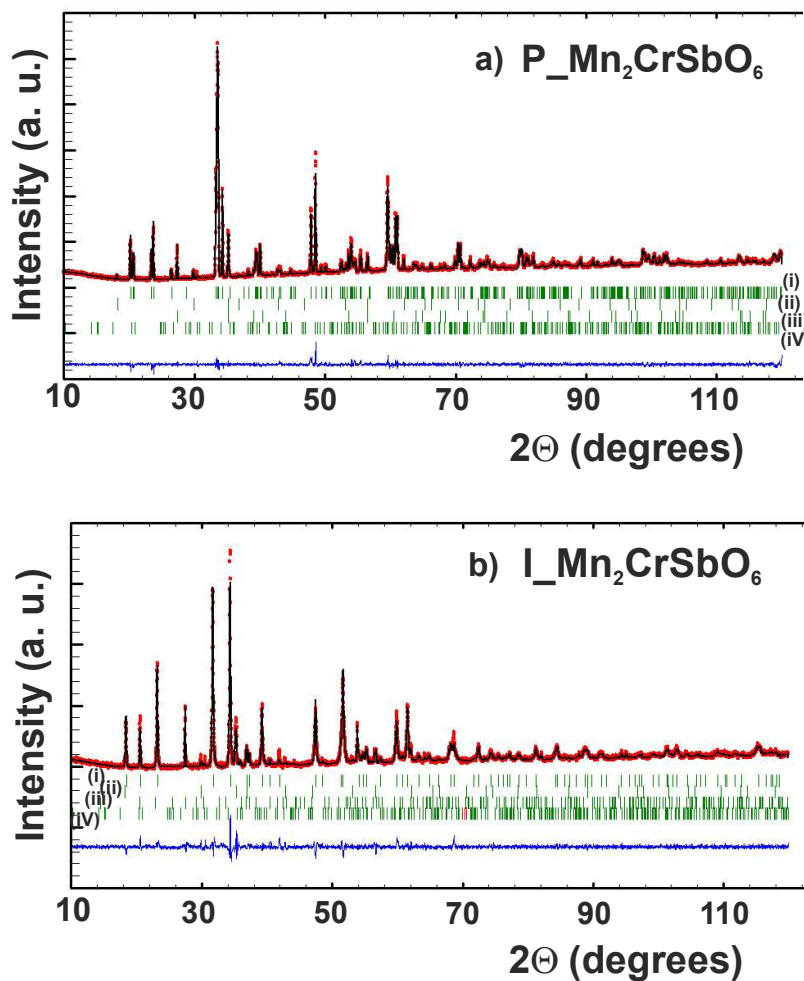ROYAL SOCIETY OF CHEMISTRY

www.rsc.org/dalton

Figure SF1. a) Rietveld refinement of the X-ray diffraction pattern of $P\_Mn_2CrSbO_6$ compound at room temperature (i). Minor secondary phases are $MnCr_2O_4$ (ii), Sb_2O_4 (iii) and $Mn_2Sb_2O_7$ (iv). b) Rietveld refinement of the PND pattern of $I\_Mn_2CrSbO_6$ (i). Impurities are $MnCr_2O_4$ (ii) and $MnSb_2O_4$ (iii) and $Mn_2Sb_2O_7$ (iv).
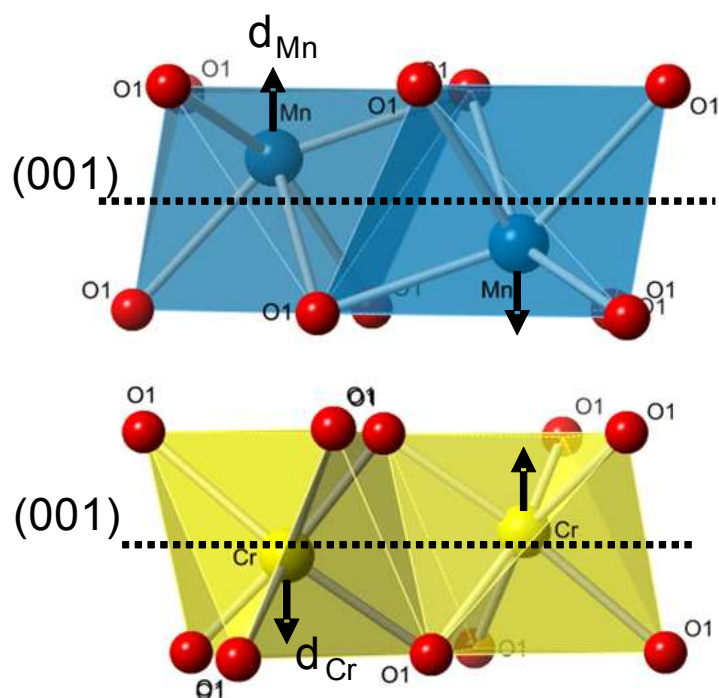
Figure SF2. Cation displacements off-centre of the octahedra due to cation-cation repulsions across shared faces and edges of octahedra.
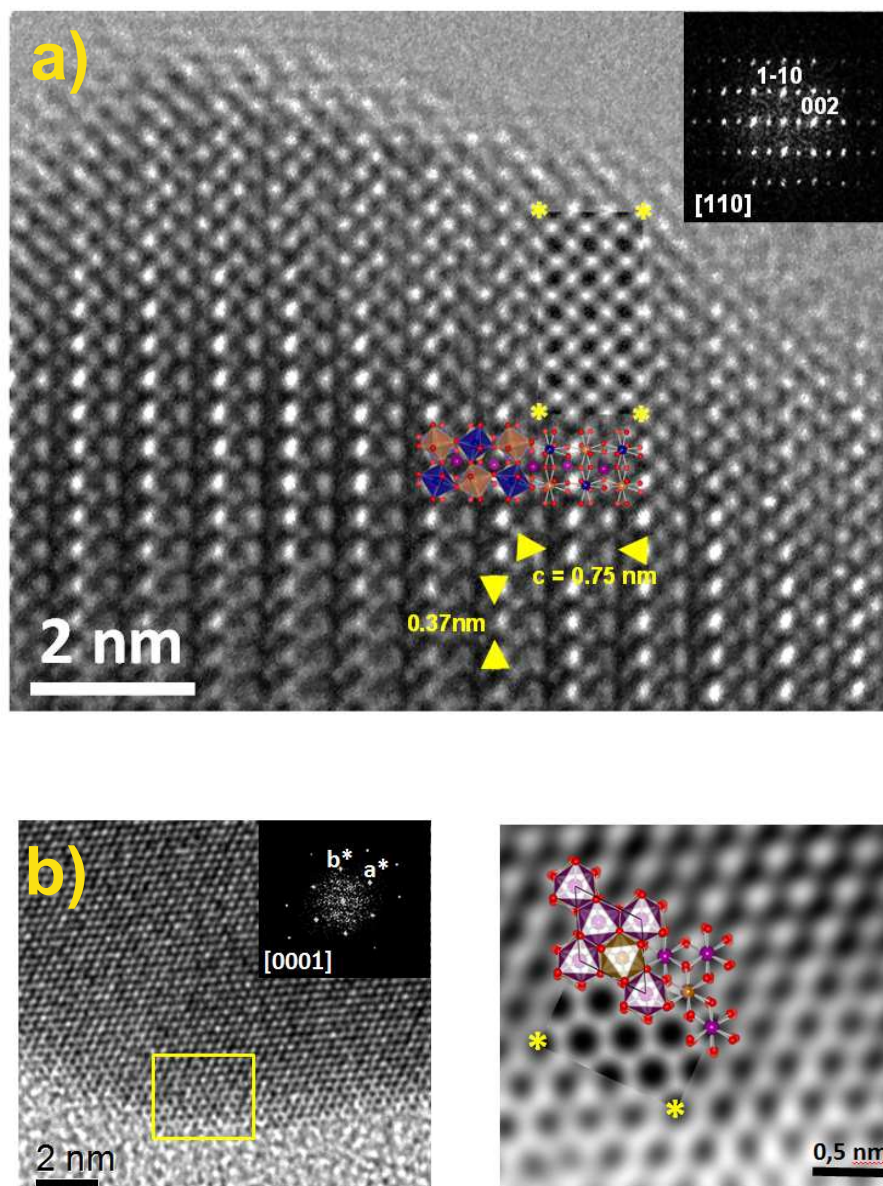
Figure SF3. HRTEM micrographs of the a) [110]p-perovskite and b) [0001]-ilmenite orientations.

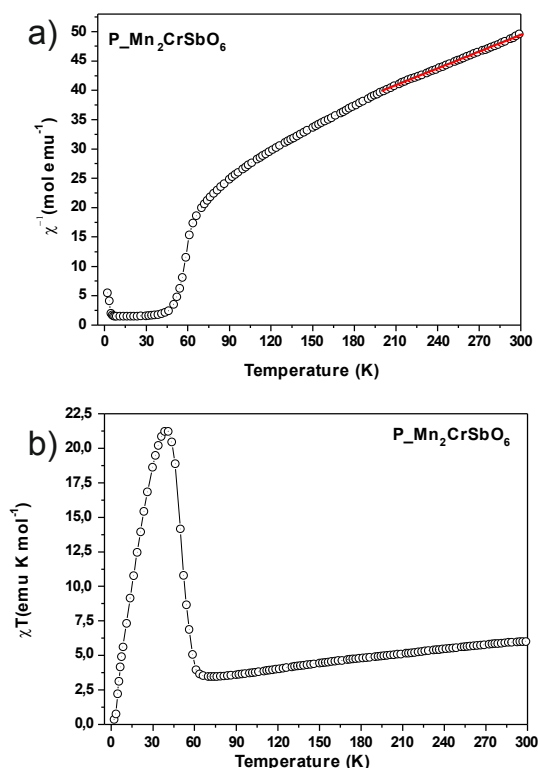**Figure SF4.** a) Temperature dependence of the reciprocal susceptibility and b) χT vs. T plot for Mn_2CrSbO_6 perovskite.
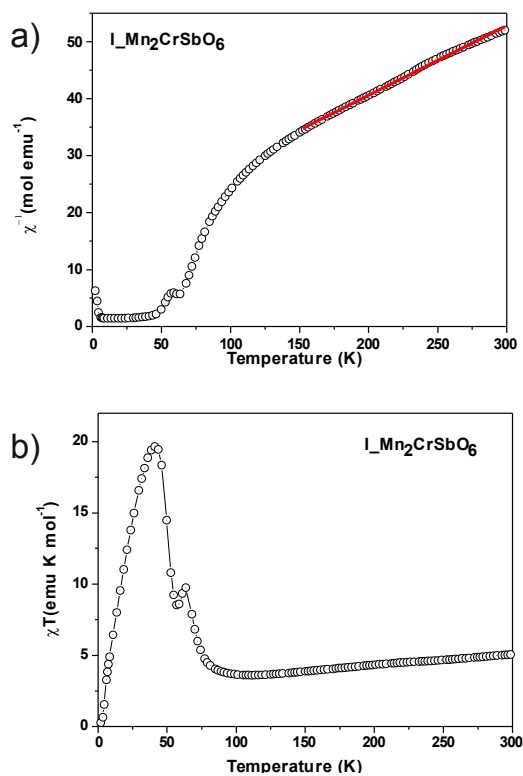
Figure SF5. a) Temperature dependence of the reciprocal susceptibility and b) χT vs. T plot for Mn_2CrSbO_6 ilmenite.
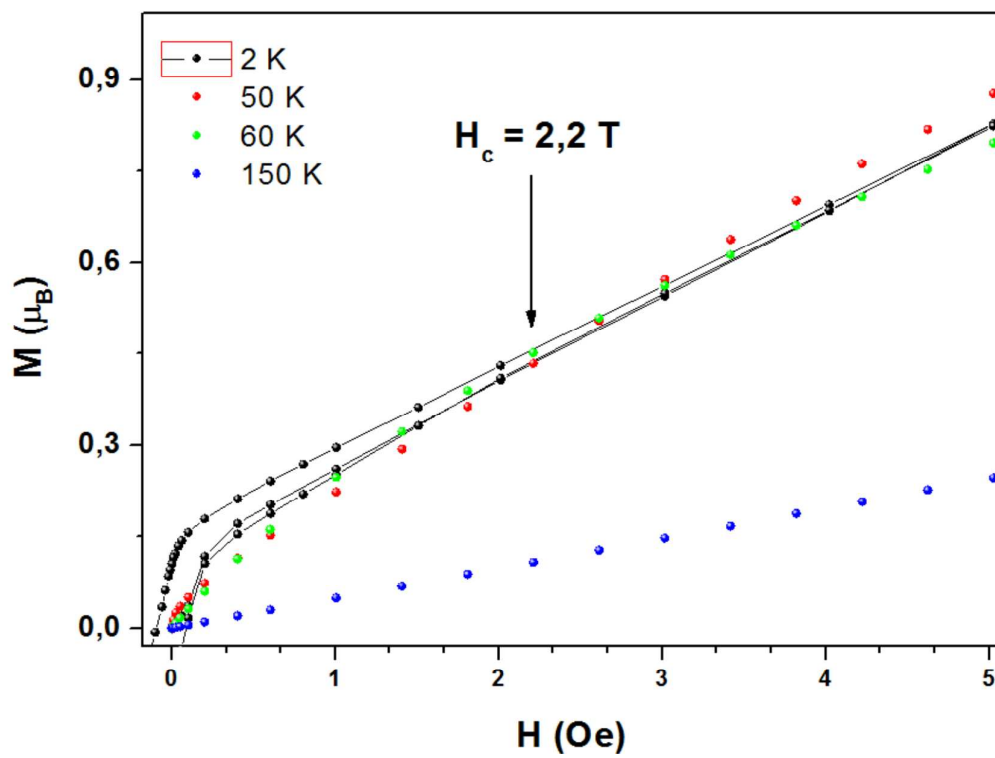
Figure SF6. Magnetization isotherms at 2, 50, 60 and 150 K temperatures. A metamagnetic transition occurs at H< 2.2 T.
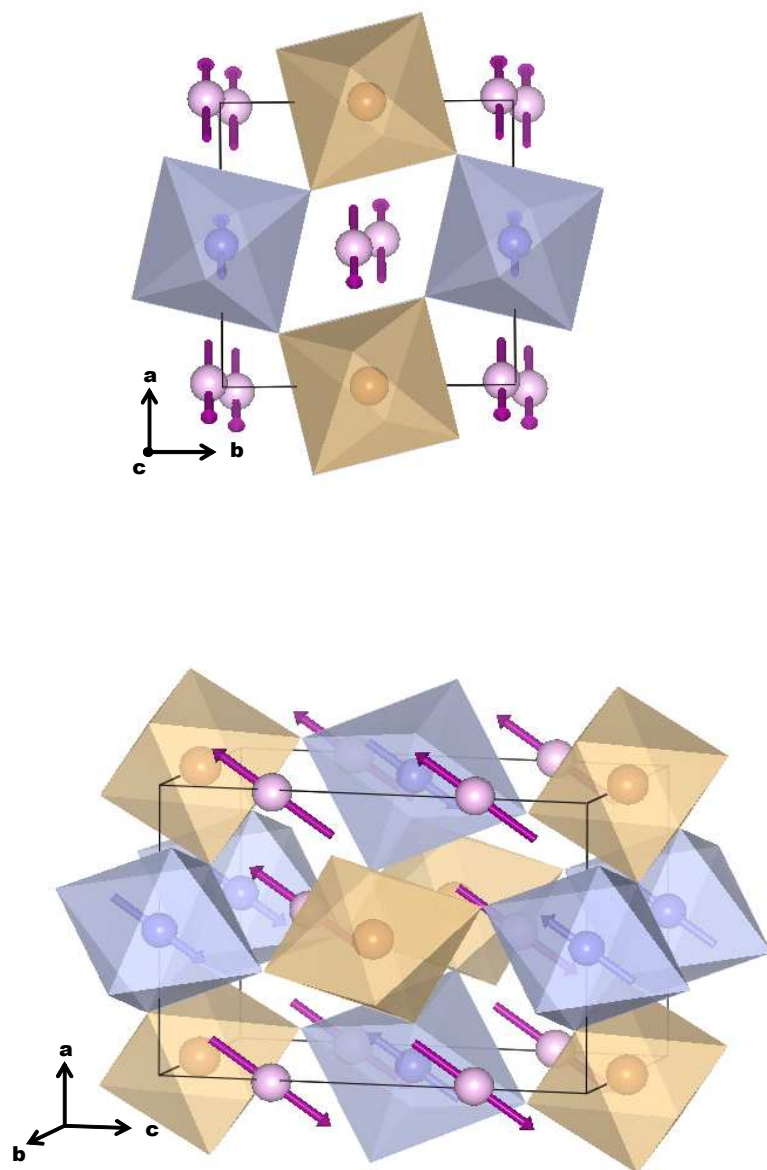
Figure SF7. Two different views of the magnetic structure for Mn$_2$CrSbO$_6$ perovskite polymorph. Magnetic moments for Mn and Cr are represented by pink and blue arrows respectively.
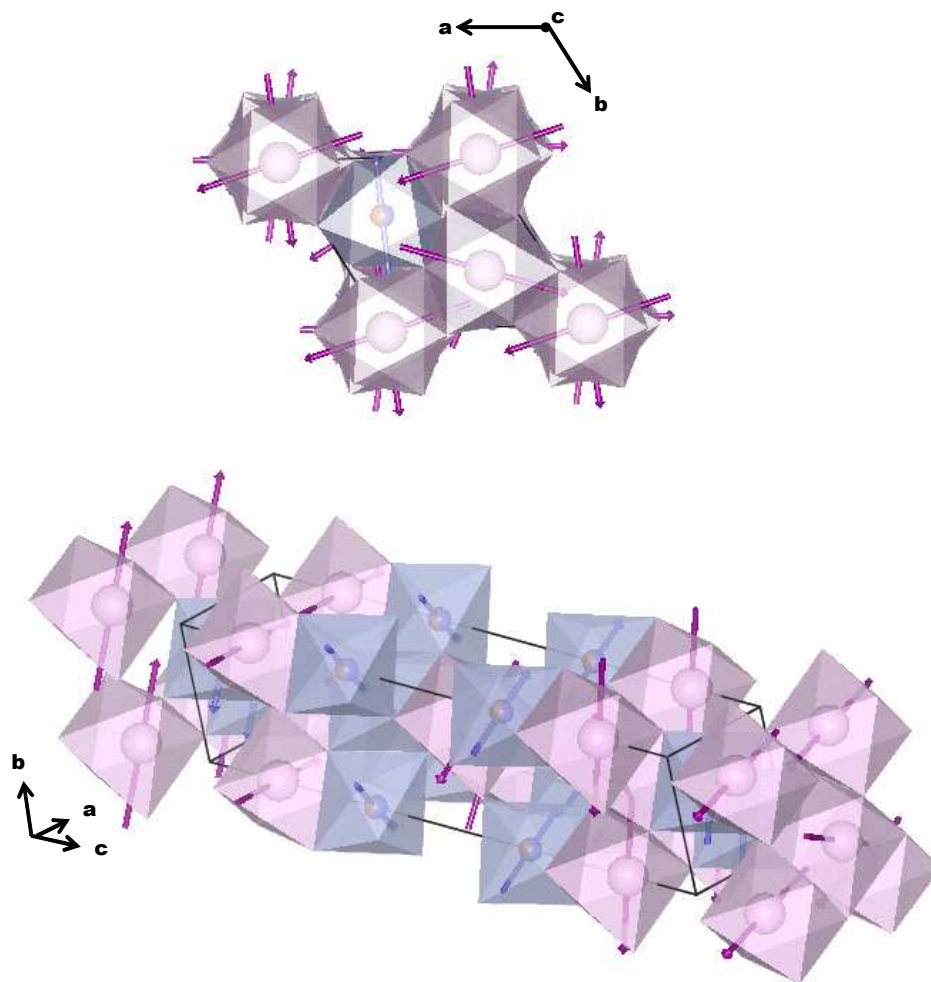
Figure SF8. Two different views of the magnetic structure for Mn_2CrSbO_6 ilmenite polymorph. Magnetic moments for Mn and Cr are represented by pink and blue arrows respectively.
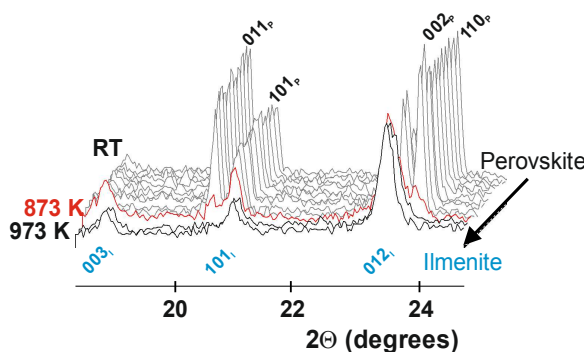
Mn_2CrSbO_6-perovskite has been synthesized at high pressure in order to stabilize the small Mn^{2+} cations on the A-perovskite site. Mn_2CrSbO_6-ilmenite polymorph can be prepared, starting from the perovskite, by a "hard-soft" phase transformation increasing the temperature at room pressure. Magnetization measurements point to AFM ground states in both compounds. However, an incommensurate magnetic ordering is present in the ilmenite modification with temperature dependence of the z-component of the propagation vector enabling a complex magnetic modulation.

Journal Name

ARTICLE

Synthesis, structures and magnetic properties of the dimorphic Mn_2CrSbO_6 oxide.

Antonio J. Dos santos-García,[a]* Elena Solana-Madruga,[b] Clemens Ritter,[c] David Ávila-Brande,[b] Oscar Fabelo,[c] and Regino Sáez-Puche.[b]

Abstract: The perovskite polymorph of Mn_2CrSbO_6 compound has been synthesized at 8 GPa and 1473 K. It crystallizes in the monoclinic $P2_1/n$ space group with cell parameters a = 5.2180 (2) Å, b = 5.3710(2) Å, c = 7.5874(1) Å and β = 90.36(1)º. Magnetic susceptibility and magnetization measurements show the simultaneous antiferromagnetic ordering of Mn^{2+} and Cr^{3+} sublattices below T_N = 55K with a small canting. Low temperature powder neutron diffraction reveals a commensurate magnetic structure with spins confined to the ac-plane and a propagation vector κ = [½ 0 ½]. The thermal treatment of this compound induces an irreversible phase transition to the ilmenite polymorph, which has been isolated at 973 K and crystallizes in R-3 space group with cell parameters a = 5.2084 (4) Å and c = 14.4000 (11) Å. Magnetic susceptibility, magnetization and powder neutron diffraction data confirm the antiferromagnetic helical ordering of spins in an incommensurate magnetic structure with κ = [0 0 0.46] below 60 K, and the temperature dependence of the propagation vector up to κ = [0 0 0.54] at about 10 K.

INTRODUCTION

Keeping up with the demands of today's society relies heavily on technological innovation and product development. The search for new materials constitutes therefore one of the fundamental aspects of Solid State Chemistry. The studied materials are usually functional, in the sense that they have some practical utility derived from the properties of the solid, that is, magnetism, ferroelectricity, superconductivity, etc. Lately, there has been a blossoming of multifunctional materials that combine two or more of these properties. In particular, multiferroic materials combine ferromagnetism and ferroelectricity, thereby allowing the control of a magnetic response through the application of an electric field[1,2]. In this context the most studied compounds are those derived from the archetypal ABO_3 perovskite which may combine two sublattices, one ferroelectrically active (d^o-closed shell cation) and the other magnetically ordered (d^n-open shell cation)[3]. The special requirement for the simultaneous presence of closed and open d-shell cations directs the search for new materials displaying both properties.[4] In this sense, high pressure has been widely used to induce phase transformations and synthesize new compounds.[5] Figure 1 shows a drawing of a set of ABO_3 compounds which, according to their Goldschmidt tolerance factor ($t = r_A + r_O /\sqrt{2} (r_B + r_O)$ where r_A, r_B and r_O are the ionic radii of A and B cations and oxygen respectively) crystallize with different crystal structures. For the ideal cubic perovskite, t is unity, although diverse distorted perovskite structures of lower symmetry can exist for values greater than 0.75 (e. g. $CaTiO_3$). However, as the size of the A-site cation

decreases relative to oxygen, the value of t decreases ($t < 0.75$) and the corundum structure (α-Al_2O_3) and its derivatives ($FeTiO_3$- and $LiNbO_3$-type) are preferred to the perovskite one. A further decrease of the size of the A-site cation leads to the more stable bixbyte polymorph (α-Mn_2O_3). When $t > 1$, AO_3 layers are hexagonal close-packed and $[BO_6]$-octahedra share faces along the hexagonal c- axis[6].
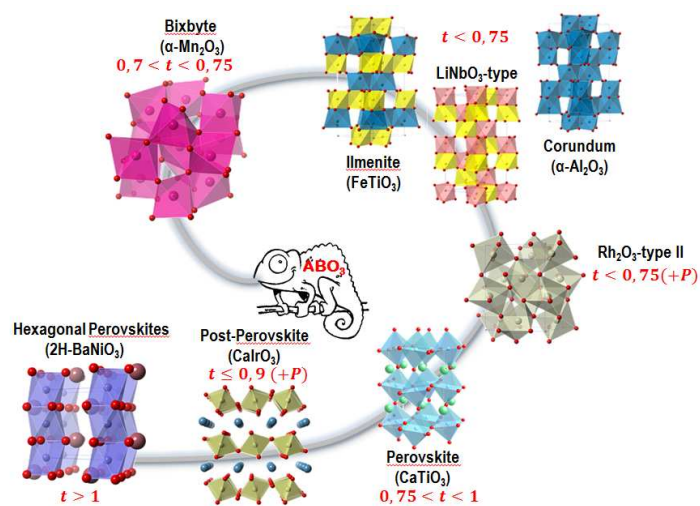

Figure 1. Symmetry adopted by ABO_3 oxides as a function of Goldschmidt tolerance factor, t. A structural type can also be accessible by high pressure phase transformation (+P).

In general, high pressure enhances steric atomic interactions and can induce transformation to denser structures.[78] For instance, corundum transforms to the Rh_2O_3-type II structure[9] and then to post-perovskite with increasing pressure[10.] The cubic bixbyte α-Mn_2O_3 transforms to a corundum-type structure at 15 GPa[11], then to a perovskite-type around 18 GPa[12] ending in the unquenchable post-perovskite-type structure above 28 GPa.[13]

Similar transformations were reported for the corundum-type Fe_2O_3[14,15,16]. $ScVO_3$ bixbyte irreversibly transforms to perovskite[17] and the non-polar $MnTiO_3$ ilmenite adopts an acentric $LiNbO_3$-type structure at moderate pressures[18,19.] Thus, high pressure represents a useful approach for tailoring new phases of ABO_3 type materials which might show the desired multifunctional behaviour at elevated temperatures.[20,21,22]

We report here the high pressure synthesis of the complex Mn_2CrSbO_6 perovskite and ilmenite derivatives (P_ Mn_2CrSbO_6 and I_ Mn_2CrSbO_6 in what follows), in which the combination of paramagnetic Cr^{3+} (d^3) – Mn^{2+} (d^5) cations with ferroelectrically active Sb^{5+} (s^0) could develop interesting interactions resulting in a possible multifunctional material.

EXPERIMENTAL SECTION

A polycrystalline specimen of the Mn_2CrSbO_6 perovskite was synthesized via the same high-pressure "Conac"-type press method used to prepare the Mn_2FeSbO_6 perovskite and ilmenite[23]. A stoichiometric mixture of Mn_2O_3, Cr_2O_3 and Sb_2O_3 was reacted inside a gold capsule at 1473 K under 8 GPa of pressure for 15 min, followed by quenching to ambient temperature and slow depressurization. The sample was initially characterized by X-ray powder diffraction with a Philips X'pert diffractometer using monochromatic Cu K-α1 radiation. The ilmenite modification could not be obtained as single phase at high pressure conditions but it can be obtained by thermal treatment in air of P_Mn_2CrSbO_6. The phase transformation from P_ Mn_2CrSbO_6 to I_ Mn_2CrSbO_6 was monitored by in-situ X-ray diffraction patterns collected from room temperature up to 1173 K at a PANalytical X'Pert PRO MPD diffractometer equipped with a high temperature Anton Paar HTK1200 chamber.

Powder Neutron Diffraction (PND) data were collected at 300 K on the high resolution D2B diffractometer and at 1.5 K using the high intensity diffractometer D1B, both at the Institute Laue Langevin, Grenoble, France. 100 mg of P_ Mn_2CrSbO_6 and I_ Mn_2CrSbO_6 were placed in sealed vanadium cans within a He cryostat. The diffraction profiles were collected at D2B in the range 2θ = 0-160° with a neutron wave length of 1.594 Å and a step-width of 0.05°; the patterns on D1B were collected between 2θ = 0-130° with a step-width of 0.1° and a neutron wave length of 2.52 Å. The temperature dependence of the ilmenite magnetic reflections was checked between 1.5 K and 94 K on the D1B diffractometer, taking a pattern about every 2 K.

The magnetic susceptibility was measured over the temperature range 2-500 K, using a superconducting quantum interference device (SQUID) XL-MPMS magnetometer under zero-field-cooling (ZFC) and field-cooling (FC) conditions, using a DC magnetic field of 1000 Oe. Magnetization measurements as a function of the applied magnetic field (H) were performed at several temperatures at magnetic fields up to 5 T. High-resolution transmission electron microscopy (HRTEM) and selected area electron diffraction (SAED) were performed on a

JEOL JEM 3000F operating at 300 kV (double tilt ±20º point resolution 1.7 Å) fitted with a X-ray energy-dispersive spectrometer (XEDS) OXFORD INCA for the compositional analysis of each investigated crystal by in situ observations. Simulations of the HRTEM images were performed with the software MacTempas X[24,] using the structure of the different polymorphs refined from neutron diffraction data.

Rietveld analysis of the profiles was carried out using the Fullprof_Suite program[25] and the magnetic symmetry analysis was performed by means of the program BasIreps[26].

RESULTS AND DISCUSSION

Structural and microstructural characterization.

Attempts to synthesize Mn_2CrSbO_6 compounds at room pressure were unsuccessful and led to the formation of the $MnCr_2O_4$, $MnSb_2O_6$ and Mn_2Sb2O_7 ternary oxides. These oxides are highly stable and coexist with ilmenite and/or perovskite phases in a broad range of pressure and temperature conditions. In fact, I_Mn_2CrSbO_6 can't be isolated as nearly single phase by solid state reaction at high pressure[27]. Otherwise, P_ Mn_2CrSbO_6, which requires the use of high pressure synthesis in order to stabilize the small Mn^{2+} cations on the A-perovskite site, was previously synthesized by Bazuev et al.[27] and can be obtained at 8 GPa. Then, I_Mn_2CrSbO_6 was obtained through the thermal treatment in air of the already prepared P_Mn_2CrSbO_6 compound. This kind of synthesis, where an already prepared high pressure material is the precursor for a following room pressure chemical process, can be described as "hard-soft" chemistry[28]. These "hard-soft" reactions alter the local chemistry or even crystal structure due to the partial instability of the high pressure phase, thus leading to unusual properties[29]. Figure 2 depicts the thermal evolution of the phase transformation from the "hard" high pressure P_Mn_2CrSbO_6 to the corresponding "soft" ilmenite I_Mn_2CrSbO_6. The perovskite starts transforming to ilmenite at 873 K, a process which is completed at temperatures up to 973 K. This phase transformation is irreversible and the I_Mn_2CrSbO_6 remains stable at room temperature.
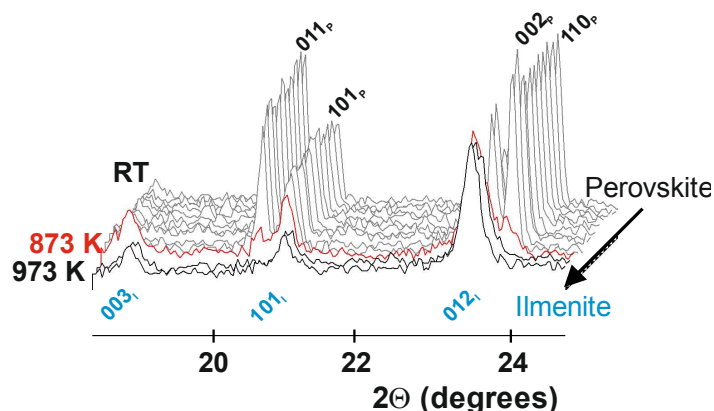
Figure 2. Magnification of XRD diagrams collected between room temperature and 973 K. Main perovskite (P) and ilmenite (I) reflections are marked.

The perovskite phase is denser than ilmenite; therefore, it is the stable structure at high pressure and temperature and can be accessible from phase transformation of ilmenite at high pressure[30,31]. However, lithium niobate-phase, but not ilmenite, appears to be the quench product of the perovskite[32,33,34]. This

is not surprising since perovskite structure can indeed be derived geometrically from $LiNbO_3$-type through a topological transformation with a continuous displacement of atoms. Surprisingly, it has been reported by Megaw that a similar transition is quite impossible for the ilmenite structure, since a cationic interchange between Mn and Cr/Sb would be needed[35]. In fact, the phase transformation from $P\_Mn_2CrSbO_6$ to $I\_Mn_2CrSbO_6$ represents the first example in the literature. Then, a rearrangement and redistribution of atoms via diffusion is required in the perovskite to ilmenite phase transformation. The transition requires high temperatures (~873 K) to aid kinetics, but the transition is clearly completed at 1 atm and 973 K (see Figure 2).

Initial X-ray diffraction suggested an ordered $P2_1/n$ perovskite structure ($\sqrt{2}a_p$ x $\sqrt{2}a_p$ x $2a_p$, where a_p is the cubic perovskite lattice parameter) for $P\_Mn_2CrSbO_6$ and the centrosymmetric R-3 space group for $I\_Mn_2CrSbO_6$ (Supplementary Figure 1, SF1). Further Rietveld refinements of neutron data were used for accurate structural determination. A small amount of $MnCr_2O_4$ (4.2 %), Sb_2O_4 (4.8 %) and $Mn_2Sb_2O_7$ (<1%) were observed in perovskite synthesis and considered in the fit. On the other hand, $MnCr_2O_4$ (4.2 %) and $MnSb_2O_4$ (4.4 %) were observed in ilmenite[36]. Plots are shown in Figure 3, and refined crystallographic parameters and agreement factors for $P\_Mn_2CrSbO_6$ and $I\_Mn_2CrSbO_6$ are summarized in Tables 1 and 2 respectively. The $P2_1/n$ parameters for $P\_Mn_2CrSbO_6$ are a = 5.2180 (2) Å, b =5.3710 (2) Å and c = 7.5874 (1) Å, β = 90.36 (1) and V = 212.642(13) $Å^3$. From the metal-oxygen distances one can see that Cr and Sb sit at the center of an octahedron. Mn-cations are placed at the perovskite A-site but are 6-fold coordinated, consistent with the small ionic radius for Mn^{2+}, which leads to a highly distorted perovskite structure.

The corresponding inset figures show the crystal structures as obtained from the refinement. The estimated distortions of the octahedra were calculated from the distortion index as $\Delta = (1/n)*\Sigma_i^n[(d_i-d_{av})/d_{av}]^2$; where d_i and d_{av} are individual and average M-O bond lengths in the polyhedron, respectively[37]. The $[SbO_6]$ octahedron is almost regular in size showing a distortion as small as 7.4 x 10^{-6}. However, the $[CrO_6]$ octahedron is highly distorted (that is, 2.7 x 10^{-4}) mainly due to the strong covalency of the Mn-O bonds and cation-cation interactions. Bond valence calculations (BVS) using an interpolation method[38] yield average charges of +1.5, 2.8 and +5.4 for Mn, Cr and Sb sites respectively.

Concerning the ilmenite modification, all the cations are in octahedral coordination (see inset of Figure 3b). Its structure can be described on the basis of the corundum structure where Mn and Cr/Sb atoms segregate onto alternate planes parallel to (0001)[39]. h0-hl reflections with l odd are systematically present in the XRD and PND diagrams, indicating the absence of a c-glide plane or disorder between Mn and Cr/Sb sites of the ilmenite structure[40]. It is rhombohedrally centered hexagonal, a = 5.2084(4) Å, c = 14.4000 (11) Å and V = 338.297(44) $Å^3$ with space group R-3. Similar to corundum, the cations are displaced off-centre of the octahedra due to cation-cation repulsions across shared faces and edges of octahedra. This results in the puckering of the cation octahedra above and below parallel to (0001). To illustrate these displacements (Supplementary Figure 2, SF2), we have calculated the deviation of the experimental cation z-parameter from their ideal values (1/6 and 1/3 for Mn- and Cr/Sb-sites respectively)[41]. These account for d_{Mn} = 0.025 Å and $d_{Cr/Sb}$ = -0.008 Å and are considerable smaller than those values reported for other ilmenites. The experimental distortion of the $[Mn-O_6]$

octahedra (1.1 x 10^{-3}) is higher than that of $[Cr/Sb-O_6]$ (2.5 x 10^{-7}), opposite of ilmenite mineral ($FeTiO_3$), where the distortion of $[Ti-O_6]$ is higher than that of $[Fe-O_6]$. Bond valence calculations (BVS) using an interpolation method[38]
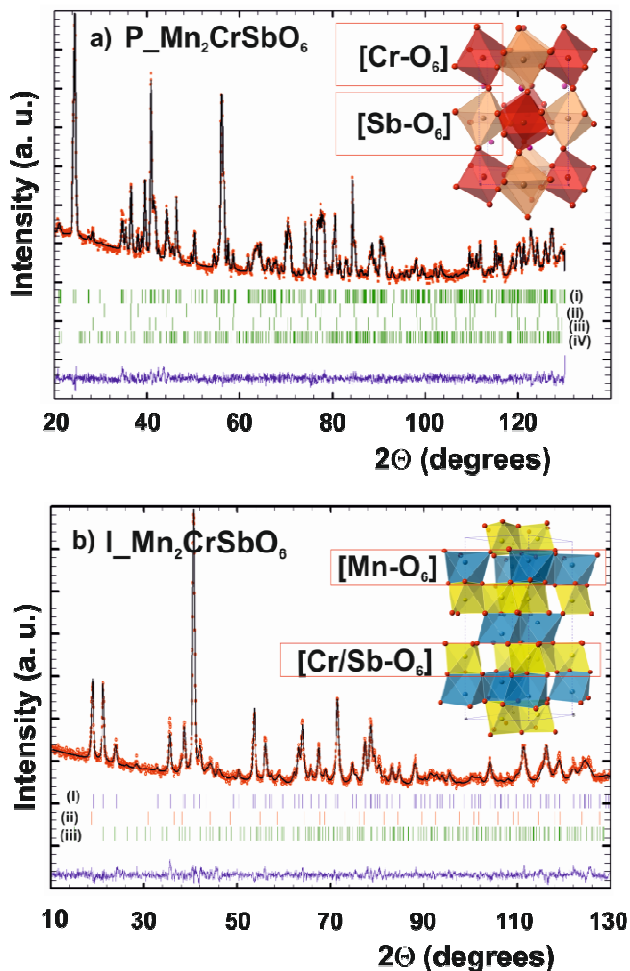
yield average charges of +1.9, 2.9 and +5.2 for Mn, Cr and Sb sites respectively, confirming the Mn^{2+}, Cr^{3+} and Sb^{5+} ionic configurations.

Figure 3. a) Rietveld refinement of the powder neutron diffraction pattern of $P\_Mn_2CrSbO_6$ compound at room temperature (i). Minor secondary phases are $MnCr_2O_4$ (ii), Sb_2O_4 (iii) and $Mn_2Sb_2O_7$ (iv). b) Rietveld refinement of the PND pattern of $I\_Mn_2CrSbO_6$ (i). Impurities are $MnCr_2O_4$ (ii) and $MnSb_2O_4$ (iii).

Further microscopic analysis of both polymorphs confirmed the adopted symmetry. High resolution transmission electron micrographs (HRTEM) along with Fast Fourier Transform-image (FFT) are depicted in Figure 4. A B-site ordered perovskite is clearly observed on the high-resolution image taken along [010] zone axis in Figure 4a. The calculated image obtained with the refined atomic coordinates of Table 1 at a thickness t = 30 Å and a defocus of -425 Å is superimposed and it is in good agreement with the experimental one. The projected structural model represents the Cr (blue spheres) and Sb (brown spheres) rock salt-type ordering in the perovskite. This type of cationic ordering is confirmed by the line profile performed along the Cr/Sb row, where a regular alternation of the contrast is clearly observed. Figure 4b shows a HRTEM image along the [2-1-10] orientation of $I\_Mn_2CrSbO_6$.

The crystallographic results summarized in Table 2 were used as input for HRTEM image simulation showing a good matching with the experimental one for a defocus value of -200 Å and a thickness of 57 Å. The variation of the contrast of the
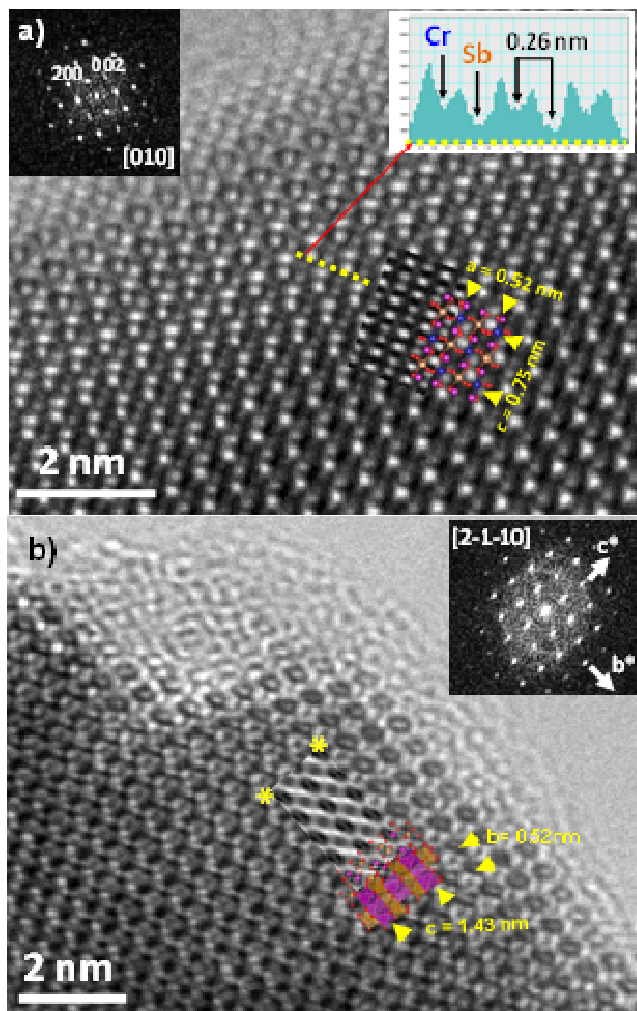

Figure 4. **High resolution electron micrographs of a) P_Mn$_2$CrSbO$_6$ along [010] and b) I_Mn$_2$CrSbO$_6$ [2-1-10] zone.**

HRTEM image, with the regular stacking of grey and dark rows, reveals the stacking sequence of Mn and Cr/Sb planes along (0001). There is no evidence of cation ordering between Cr and Sb within the (01-10) planes. Therefore, the period observed in both experimental and calculated images corresponds well with an ilmenite-type structure. A schematic representation of the structure of I_Mn$_2$CrSbO$_6$ is superimposed. Supplementary Figure 3, SF3, shows additional HRTEM micrographs of the [110]p-perovskite and [0001]-ilmenite orientations.

Magnetic properties.
Figure 5 shows the temperature dependence of ZFC and FC magnetic susceptibilities under a field of 1000 Oe for P_Mn$_2$CrSbO$_6$ (Figure 5a) and I_Mn$_2$CrSbO$_6$ (Figure 5b). For the perovskite the susceptibility rises sharply below ~55 K and the ZFC-curve presents a rounded maximum centred at ~20 K.

The ZFC data diverge from the FC data below this temperature. The reciprocal ZFC data (Supplementary Figure 4, SF4) were fitted between 200 and 300 K with the Curie-Weiss law, $\chi(T) = C/(T-\theta)$, resulting in $\theta = -219.7(1)$ K and $C = 10.5$ (1) emuKmol-1, implying a total effective moment of $\mu_{eff} = 9.2(1)$ μ_B which agrees well to that expected for the 2Mn^{2+} (S=5/2) and Cr^{3+} (S=3/2) contributions.

Table 1. **Crystallographic parameters, selected interatomic distances (Å) and angles (°) for P_Mn$_2$CrSbO$_6$ at 300 K.[a]**

a (Å)	b (Å)	c (Å)	β (°)		
5.2180 (2)	5.3710(2)	7.5874(1)	90.36(1)		
Atom	Site	x	y	z	Occ
Mn	4e	0.0149(8)	0.0471(7)	0.7463(7)	1
Cr	2d	½	0	0	1
Sb	2c	0	½	0	1
O1	4e	0.3116(7)	0.3073(9)	0.9386(5)	1
O2	4e	0.3143(6)	0.3073(9)	0.5640(4)	1
O3	4e	0.8788(5)	0.4454(5)	0.7540(4)	1
Mn-O$_1$	2.539(6)	(Cr-O$_1$)×2	1.975(5)	(Sb-O$_1$)×2	1.986(4)
Mn-O$_1$	2.113(6)	(Cr-O$_2$)×2	1.997(4)	(Sb-O$_2$)×2	1.976(4)
Mn-O$_2$	2.517(6)	(Cr-O$_3$)×2	2.053(3)	(Sb-O$_3$)×2	1.989(3)
Mn-O$_2$	2.123(6)				
Mn-O$_3$	2.255(5)				
Mn-O$_3$	2.126(5)				
d$_{av}$ Mn-O	2.278(2)	d$_{av}$ Cr-O	2.008(2)	d$_{av}$ Sb-O	1.984(2)
		Δ[CrO$_6$]	2.7 x 10^{-4}	Δ[SbO$_6$]	7.4 x 10^{-6}
BVS(Mn)[b]	1.5	BVS (Cr)	2.8	BVS (Sb)	5.4
Mn-O$_1$-Cr	88.7(3); 116.8(3)	Mn-O$_2$-Cr	84.8(2); 101.0 (3)	Mn-O$_3$-Cr	90.7(2); 105.4 (3)

[a] Fitting residuals R_p=2.31%, R_{wp}=2.86%, R_B=4.89% and R_F=3.89%,. [b]$V_i = \Sigma_j S_{ij}i = \exp(r_0 - r_{ij}/0.37)$. Values calculated using r_{ij}= 1.79 for Mn^{2+}, 1.724 for Cr^{3+} and 1.942 for Sb^{5+}.

Table 2. Crystallographic parameters, selected interatomic distances (Å) and angles (°) for I_Mn$_2$CrSbO$_6$ at 300 K.[a]

a (Å)	b (Å)	c (Å)	γ (°)		
5.2084 (4)	5.2084 (4)	14.4000(11)	120		
Atom	Site	x	y	z	Occ
Mn	6c	0	0	0.1411(5)	1
Cr/Sb	6c	0	0	0.3408(5)	0.5/0.5
O1	18f	0.2875(4)	-0.0285(5)	0.2560(2)	1
(Mn-O)×2	2.286(6)	(Cr-O)×2	1.994(5)	(Sb-O)×2	1.994(5)
(Mn-O)×2	2.139(4)	(Cr-O)×2	1.992(4)	(Sb-O)×2	1.992(4)
d$_{av}$ Mn-O	2.212(2)	d$_{av}$ Cr-O	1.993(2)	d$_{av}$ Sb-O	1.993(2)
Δ[MnO$_6$]	1.1 x 10^{-3}	Δ[CrO$_6$]	2.5 x 10^{-7}	Δ[SbO$_6$]	2.5 x 10^{-7}
BVS(Mn)[b]	1.9	BVS (Cr)	2.9	BVS (Sb)	5.2
Mn-O-Mn	91.3(1)	Mn-O-Cr	119.6(3); 126.5(3)		

[a] Fitting residuals R_p=3.51%, R_{wp}=4.46%, R_B=3.79% and R_F=2.38%,. [b]$V_i = \Sigma_j S_{ij}i = \exp(r_0 - r_{ij}/0.37)$. Values calculated using r_{ij}= 1.79 for Mn^{2+}, 1.724 for Cr^{3+} and 1.942 for Sb^{5+}.

According to the negative Weiss constant, it is reasonable to assign the maximum centred at ~ 20 K to an AFM ordering transition with a small contribution of a weak-ferromagnetic component, as demonstrated by field dependent magnetization measurements at different temperatures (see inset of Figure 5a). This ferromagnetic component may arise from the effect of symmetry-allowed canting of the antiferromagnetically coupled Cr and Mn spins below $T_N \approx 55$ K. In fact, this AFM ordering is due to the simultaneous ordering of the Mn^{2+} and Cr^{3+} magnetic sublattices, which has been determined by neutron diffraction experiments at 2 K and will be described below in the magnetic-structure determination section.
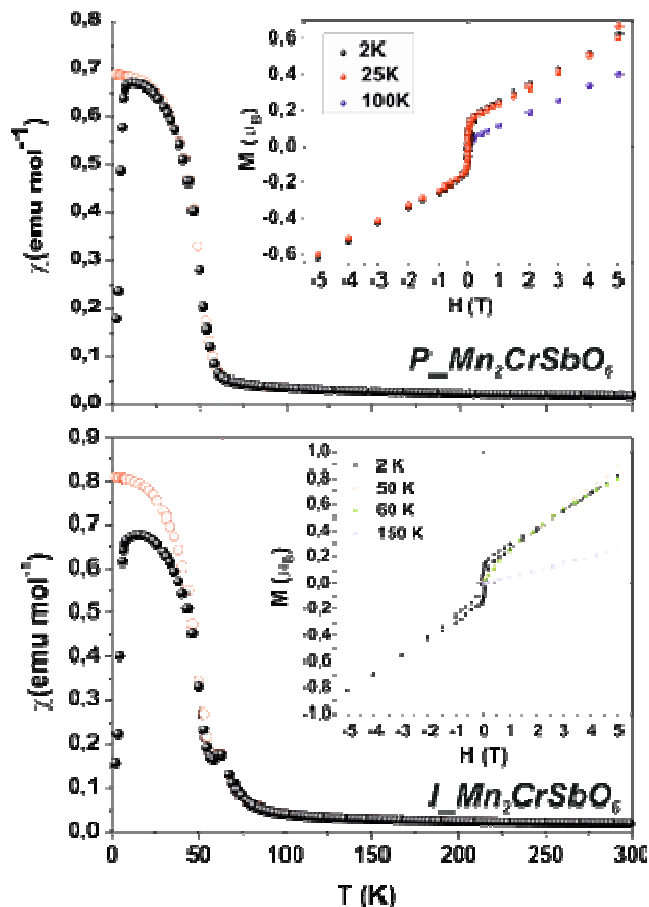

Figure 5. a) Zero-field cooled (black closed circles) and field-cooled (red open circles) dc-susceptibility data of P_Mn$_2$CrSbO$_6$ along with the M(H) data at different temperatures b) corresponding magnetic characterization for the ilmenite compound.

The magnetic behaviour of the corresponding I_Mn$_2$CrSbO$_6$ looks similar to that observed for the perovskite polymorph. However, a careful examination of the data reveals the existence of a first T_{N1} transition around 60 K followed by a consecutive transition T_{N2}, at lower temperatures, which is almost coincident to that observed in the perovskite. A small, but not negligible difference below the T_N values is evident in the enlargement of the FC curves. Accordingly, a small hysteresis in the 2 K magnetization vs applied field loop (See inset of Figure 5b) with a small remanent magnetization of $\approx$ 0.08 μ_B and a coercive field of $\approx$ 300 Oe confirms the presence of a noticeable ferromagnetic contribution for the ilmenite. The fitting of the inverse ZFC plot (Supplementary Figure 5, SF5)

with the Curie-Weiss law gives a magnetic moment of $\mu_{eff} =$ 8.8(1) μ_B and a Weiss temperature of $\theta = -195.6(1)$ K which points to an AFM ground state. The antiferromagnetic correlations are confirmed by the presence of metamagnetism in the M vs. H measurements (inset of Figure 5b, and Supplementary Figure 6, SF6). At a critical field of 2.2 T, the system adopts a different configuration and the sublattice magnetizations ($\uparrow M^+$ and $\downarrow M^-$) get progressively switched until they line up with the applied magnetic field.[42] Taking the susceptibility and neutron diffraction data together, we are in the position to say that the magnetic order of the ilmenite differs from that of the perovskite. In fact, we can assume that the magnetic phase transition observed at $T_1 \sim 60$ K is due to an elliptical-helix ordering of the Mn and Cr cations followed by a temperature dependence of the propagation vector.

Magnetic structures.
The difference between the profiles collected at 2 (below T_N) and 80K (well above T_N) for P_Mn$_2$CrSbO$_6$ on the D2B diffractometer with high resolution (1.594 Å) is shown in Figure 6. Assuming the structural P2$_1$/n model, the magnetic reflections can be indexed by the magnetic propagation vector κ = [½ 0 ½]. Magnetic symmetry analysis using the program BASIREPS was performed to determine the allowed irreducible representations (IR) and their basis vectors (BV). Mn and Cr reside at 4e and 2d Wyckoff sites but follow the same IR. Both Mn and Cr have two non-zero basis vectors. As the values for the coefficients were very similar, they were constrained to the same value, thereby reducing the number of magnetic parameters: one for Mn and one for Cr. The moments are coupled antiferromagnetically to their nearest-neighbours within (101) planes. A general view of the magnetic structure is depicted in the inset of Figure 6. The magnetic moments at 2 K amount to about 4.8(1) μ_B for Mn (pink arrows) and 2.7(1) μ_B for Cr (blue arrows). Different views of the magnetic structure are depicted in Supplementary Figure 7, SF7.
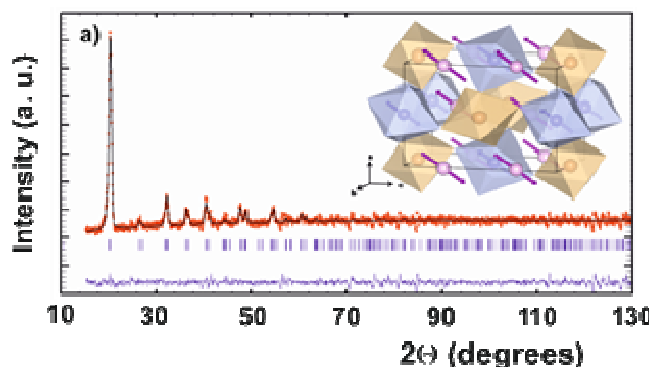

Figure 6. Rietveld refinement of the difference pattern between the 2 and 80K neutron diffraction data of P_Mn$_2$CrSbO$_6$. Tick marks correspond to magnetic reflections. The inset shows the schematic representation of the magnetic structure at 2 K.

Figure 7 displays the low-angle region of the neutron diffraction patterns showing the thermal evolution (thermodiffractogram) of I_Mn$_2$CrSbO$_6$ between 1.5 and 94 K as measured on D1B using $\lambda = 2.52$ Å. Some additional broad diffuse intensity appears already at $T_{N1} = 60$ K, however, only below $T_{N2} = 55$ K it is possible to clearly discern new magnetic peaks. These new magnetic reflections can be indexed at 55 K with the propagation vector $\kappa_{HT} = [0\ 0\ \sim 0.46]$. On lowering the

temperature the wave vector increases smoothly to reach below about 10 K a value of κ_{LT}= [0 0 0.54]. Figure 7b shows the contour plot of the incommensurate magnetic reflection [0 0 κ] below 55 K. Changes in the value of the propagation vector with temperature, depicted in Figure 7c, have been evaluated by Rietveld refinement of the data collected between 55 K and 1.5 K. It can be seen that the evolution of κ_z does not show any discontinuity while passing through the commensurate value of ½. Magnetic symmetry analysis using BASIREPS[26] shows that in space group R-3 with κ = [0 0 κ_z] there are 3 allowed irreducible representations (IR) for the Wykoff site $6c$ where both cations Mn and Cr are situated.
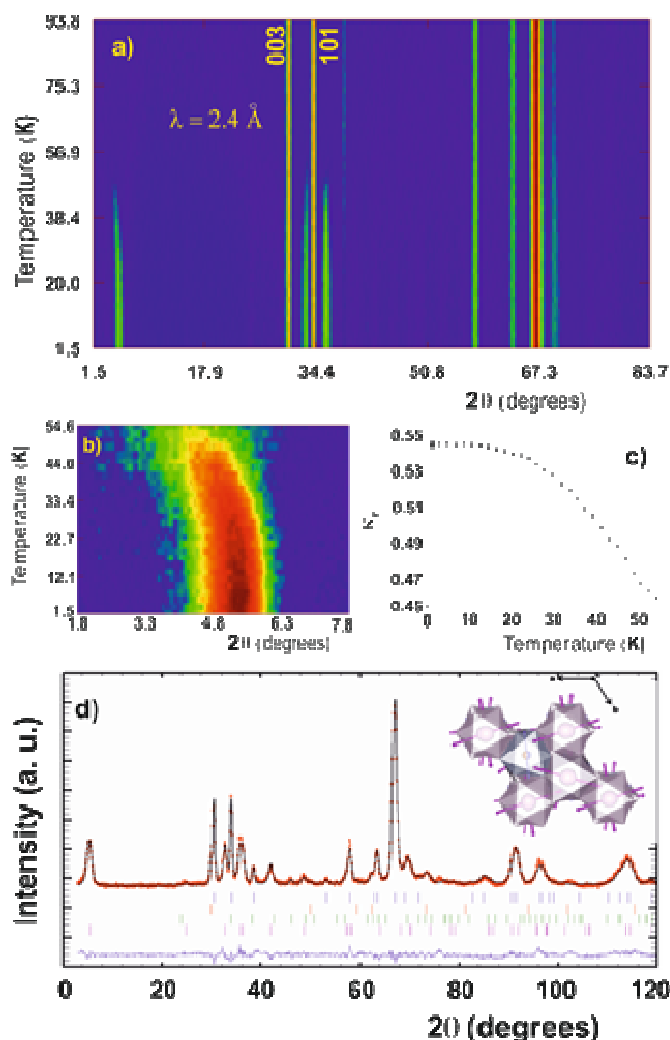

Figure 7. a) Part of the thermodiffractogram collected at λ = 2.4 Å between 1.5 and 94 K. b) Temperature variation of the magnetic Bragg peak position c) Temperature dependence of the z-component of the propagation vector. d) Rietveld refinement of the PND-pattern taken at 2 K. First and last rows of Bragg intensities correspond to the nuclear and magnetic structures for I_Mn$_2$CrSbO$_6$ respectively. The 2nd and 3rd rows stem from Bragg reflections from minor MnCr$_2$O$_4$ and MnSb$_2$O$_4$ impurities, respectively. The inset shows the schematic representation of the magnetic structure at 2 K.

All three IRs have only one basis vector: two describe a helical ordering within the hexagonal basal plane while the third one

corresponds to a cycloidal modulation along the direction of the propagation vector i.e. the c-axis. Apart from the relation between sites coupled through the R-centring there are no constraints for the coupling of the magnetic moments within the unit cell. This means that the cations on the Wykoff site $6c$ are split into two independent orbits giving two independent Mn and two independent Cr moments on [0 0 z] and [0 0 –z]. The refinement of the neutron data clearly indicates that the cycloidal magnetic structure is not able to account for the measured magnetic intensities. However, assuming a helical magnetic ordering of all 4 independent cation sublattices makes the refinement converge quickly. As the refined magnetic moments for the two independent Mn and the two independent Cr spins adopt respectively very similar values they were constrained to be equal. Refining the phase shifts between the two Mn-orbits and the two Cr-orbits leads to a final refinement using only 4 intensity related parameters. It is not possible to distinguish between the two IRs describing this helical magnetic structure. In fact they represent the two different chiral descriptions of the helix which only differ in the sense of rotation of the helix in c-direction. Figure 7d shows the Rietveld refinement of the PND data taken at 2 K on the D1B diffractometer. The magnetic ground state of the incommensurate helical-spin ordering of Mn (pink arrows) and Cr (blue arrows) cations, with κ_{LT}= [0 0 0.54], running along the c-axis is depicted in a view perpendicular to the (001) plane in the inset of Figure 7d (Different views of the magnetic structure are depicted in Supplementary Figure 8, SF8). The magnetic moment values amount to μ_{Mn} = 3.1(1) μ_B and μ_{Cr} = 1.7(1) μ_B and are therefore significantly reduced when compared to the expected values of about 5 μ_B and 3 μ_B for Mn^{2+} and Cr^{3+}. This can be explained by the structural details of this modification where the closest cation-cation interaction is in fact no longer the direct Mn-Mn interaction as in the perovskite modification but along the Mn-Cr pathway with, however, half of the Cr-sites occupied by non-magnetic Sb^{+5}.

Conclusions.

Mn$_2$CrSbO$_6$ perovskite and ilmenite polymorphs require high pressure to be synthesized. Ilmenite can be stabilized at low pressures but perovskite needs 8 GPa to be prepared. Powder neutron diffraction measurements show an ordered B-site distribution of Cr and Sb cations with a monoclinically distorted perovskite structure. An Ilmenite polymorph has been also identified due to the ordering of Mn and Cr/Sb cations onto alternate planes parallel to (0001). HRTEM images demonstrate well-ordered structures free from defects. Magnetization measurements point to AFM ground states in both compounds. Magnetic structure determinations confirm the AFM behaviour in the perovskite compound. However, an incommensurate magnetic ordering is present in the ilmenite modification. The experimental results demonstrated a continuous phase transition with a temperature dependence of the z-component of the propagation vector enabling a complex magnetic modulation where the position of the magnetic Bragg peaks becomes incommensurate displaying temperature dependence.

Acknowledgements

Notes and references

Author information

[a] Departamento de Ingeniería Mecánica, Química y Diseño Industrial, E.T.S.I.D.I, Universidad Politécnica de Madrid, 28012, Spain.

[b] Departamento de Química Inorgánica, Facultad de Ciencias Químicas, Universidad Complutense de Madrid, 28040, Spain.

[c] Institut Laue-Langevin, 38042 Grenoble Cedex, France.

Corresponding Author

* To whom correspondence should be addressed.
E-mail: aj.dossantos@upm.es. (A.J.D)

Author Contributions

The manuscript was written through contributions of all authors

†Electronic Supplementary Information (ESI) available: XRD data, HRTEM micrographs in different orientations, magnification of the M(H) data for ilmenite compound, reciprocal susceptibility and χT *vs* T plots as well as different views of[43] magnetic structures. See DOI: 10.1039/b000000x/

[1] D. I..Khomskii, *J. Magn. Magn. Mater*. 2006, **306**, 1.

[2] Y. Tokura, S. Seki, N. Nagaosa, *Rep. Prog. Phys.* 2014, **77**, 076501.

[3] G. Catalan, J. F. Scott, *Adv. Mater.* 2009, **21**, 2463.

[4] A. Aimi, D. Mori, K. Hiraki, T. Takahashi, Y.J. Shan, Y. Shirako, J. Zhou, Y. Inaguma, *Chem. Mater.*, 2014, **26** (8), 2601.

[5] J. A. Rodgers, A. J. Williams, J. P. Attfield, *Z. Naturforsch.* 2006, **61b**, 1515-1526.

[6] R.H Mitchell,. *Perovskites: modern and ancient.* Almaz Press Inc. **2002**.

[7] A.A. Belik, W. Yi, *J. Phys.: Condens. Matter.* 2014, **26**, 163201.

[8] W.Grochala, R. Hoffmann, J. Feng, N. W. Ashcrofti, *Angew. Chem. Int. Ed..* 2007, **46**, 3620.

[9] J. F. Lin, O. Degtyareva, C. T. Prewitt, P. Dera, N. Sata, E. Gregoryanz, H. K. Mao, R. Hemley, *J. Nat. Mater.* 2004, **3**, 389.

[10] A. R. Oganov, S. Ono, *Proc. Nat. Acad. Sci.* 2005, **102**, 10828.

[11] S.V. Ovsyannikov, A.M. Abakumov, A.A. Tsirlin, W. Schnelle, R. Egoavil, J. Verbeeck, G. Van Tendeloo, K.V. Glazyrin, M. Hanfland, L. Dubrovinsky, *Angew. Chem. Int. Ed.* 2013, **52**, 1494.

[12] T. Yamanaka, T. Nagai, T. Okada, T. Fukuda, *Z. Kristallogr.* 2005, **220**, 938 .

[13] J. Santillan, S.H. Shim, G. Shen, V.G. Prakapenka, *Geophys. Res. Lett.* 2006, **33**, L15307.

[14] M. Pasternak, G. K. Rozenberg, G. Y. Machavariani, O. Naaman, R. D. Taylor, R. Jeanloz, *Phys. Rev. Lett.* 1999, **82**, 4663.

[15] J. S. Olsen, C. S. G. Cousins, L. Gerward, H. Jhans, B. Sheldon, *J. Phys. Scr.* 1991, **43**, 327.

[16] S. Ono, Y. Ohishi, *J. Phys. Chem. Solids* 2005, **66**, 1714.

[17] E. Castillo-Martínez, M. Bieringer, S.P. Shafi, L. M. D. Cranswick, M. A. Alario-Franco, *J. Am. Chem. Soc.* 2011, **133**, 8552.

[18] J. Ko, C. Prewitt, *Phys Chem. Mineral.* 1988, **15**, 355.

[19] N.L. Ross, J. Ko, C.T. Prewitt, *Phys Chem. Mineral.* 1989, **16**, 621.

[20] T. Kawamoto, K. Fujita, I. Yamada, T. Matoba, S.J. Kim, P. Gao, X. Pan, S.D. Findlay, C. Tassel, H. Kageyama, A.J. Studer, J. Hester, T. Irifune, H. Akamatsu, K. Tanaka, *J. Am. Chem. Soc.* 2014, **136**,15291.

[21] M.R. Li, P.W. Stephens, M. Retuerto, T. Sarkar, C.P. Grams, J. Hemberger, M.C. Croft, D. Walker, M. Greenblatt, *J. Am. Chem. Soc.*, 2014, **136** (24), 8508.

[22] E. Gilioli, L. Ehm, *IUCrJ.* 2014, **1**,590.

[23] A. J. Dos santos-García, C. Ritter, E. Solana-Madruga, R. Sáez-Puche, *J. Phys.: Condens.Matter.* 2013, **25**, 206004.

[24] Mac Tempas X. Version 2.3.7. A program for simulating HRTEM images and diffraction patterns.

[25] J. Rodriguez-Carvajal, *Physica B.* 1993, **192**, 55.

[26] C. Ritter, *Solid State Phenomena* 2011, **170**, 263.

[27] G. Bazuev, B. Golovkin, N. Lukin, N. Kadyrova, Y. Zainulin, *J. Solid State Chem*. 1996, **124**, 333.

[28] J. Gopalakrishnan, *Chem. Mater.* 1995, **7**, 1265.

[29] A. M. Arévalo-López, J. A. Rodgers, M. S. Senn, F. Sher, J. Farnham, W. Gibbs, J. P. Attfield, *Angew. Chem. Int. Ed.* 2012, **51**, 10791.

[30] A.M Arévalo-López, J.P. Attfield, *Phys.Rev.B.*, 2013, **88**, 104416.

[31] H. Mizoguchi, P. M. Woodward, S-H. Byeon, J. B. Parise, *J. Am. Chem. Soc.* 2004, **126**, 3175.

[32] A. Navrotsky, *Chem. Mater.* 1998, **10**, 2787.

[33] Y. Inaguma, K. Tanaka, T. Tsuchiya, D. Mori, T. Katsumata, T. Ohba, K. Hiraki, T. Takahashi, H. Saitoh, *J. Am. Chem. Soc.* 2011, **133**, 16920.

[34] H. Yusa, M. Akaogi, N. Sata, H. Kojitani, R. Yamamoto, Y. Ohishi, *Phys.Chem. Miner.* 2006, **33**, 217.

[35] H.D. Megaw, *Ferroelectricity in crystals.* **1957**.

[36] H. Fjellvag, A. Kjekshus,, *Acta Chem. Scand. A* 1985, **39**, 389.

[37] J.A. Alonso, M.J. Martínez-Lope, M.T. Casais, *Inorg. Chem.* 2000, **39***,* 917.

[38] J. P. Attfield, *Solid State Sci.* 2006, **8**, 861-867.

[39] B. G. Hyde, S. Andersson. *Inorganic crystal structure.* **1989**.

[40] C. A. Hoel, J. M. Gallardo Amores, E. Morán, M.A. Alario-Franco, J.-F. Gaillard, K. R. Poeppelmeier, *J. Am. Chem. Soc.* 2010, **132**, 16479.

[41] R. P. Liferovich, R. H. Mitchell, *Phys. Chem. Minerals* 2005, **32**, 442.

[42] S. Blundell, *Magnetism in condensed matter.* Oxford University Press. **2001**.

Dalton Transactions Accepted Manuscript